

2023

FiNuTyper: Design and Validation of an Automated Deep Learning-Based Platform for Simultaneous Fiber and Nucleus Type Analysis in Human Skeletal Muscle

August Lundquist
Karolinska Institutet


Enikő Lázár
Karolinska Institutet

Nan S. Han
Karolinska Institutet

Eric B. Emanuelsson
Karolinska Institutet

Stefan M. Reitzner
Karolinska Institutet

Follow this and additional works at: https://digital.sandiego.edu/engineering_facpub

 See next page for additional authors
Part of the [Engineering Commons](#)

Digital USD Citation

Lundquist, August; Lázár, Enikő; Han, Nan S.; Emanuelsson, Eric B.; Reitzner, Stefan M.; Chapman, Mark A.; Shirkova, Vera; Alkass, Kanar; Druid, Henrik; Petri, Susanne; Sundberg, Carl J.; and Bergmann, Olaf, "FiNuTyper: Design and Validation of an Automated Deep Learning-Based Platform for Simultaneous Fiber and Nucleus Type Analysis in Human Skeletal Muscle" (2023). *School of Engineering: Faculty Scholarship*. 39.

https://digital.sandiego.edu/engineering_facpub/39

This Article is brought to you for free and open access by the School of Engineering at Digital USD. It has been accepted for inclusion in School of Engineering: Faculty Scholarship by an authorized administrator of Digital USD. For more information, please contact digital@sandiego.edu.

FiNuTyper: Design and Validation of an Automated Deep Learning-Based Platform for Simultaneous Fiber and Nucleus Type Analysis in Human Skeletal Muscle

Abstract

Aim While manual quantification is still considered the gold standard for skeletal muscle histological analysis, it is time-consuming and prone to investigator bias. To address this challenge, we assembled an automated image analysis pipeline, FiNuTyper (Fiber and Nucleus Typer). **Methods** We integrated recently developed deep learning-based image segmentation methods, optimized for unbiased evaluation of fresh and postmortem human skeletal muscle, and utilized SERCA1 and SERCA2 as type-specific myonucleus and myofiber markers after validating them against the traditional use of MyHC isoforms. **Results** Parameters including cross-sectional area, myonuclei per fiber, myonuclear domain, central myonuclei per fiber, and grouped myofiber ratio were determined in a fiber-type-specific manner, revealing that a large degree of sex- and muscle-related heterogeneity could be detected using the pipeline. Our platform was also tested on pathological muscle tissue (ALS and IBM) and adapted for the detection of other resident cell types (leucocytes, satellite cells, capillary endothelium). **Conclusion** In summary, we present an automated image analysis tool for the simultaneous quantification of myofiber and myonuclear types, to characterize the composition and structure of healthy and diseased human skeletal muscle.

Disciplines

Engineering

Creative Commons License












This work is licensed under a [CC BY-NC License](https://creativecommons.org/licenses/by-nc/4.0/)

Author(s)

August Lundquist, Enikő Lázár, Nan S. Han, Eric B. Emanuelsson, Stefan M. Reitzner, Mark A. Chapman, Vera Shirkova, Kanar Alkass, Henrik Druid, Susanne Petri, Carl J. Sundberg, and Olaf Bergmann

FiNuTyper: Design and validation of an automated deep learning-based platform for simultaneous fiber and nucleus type analysis in human skeletal muscle

August Lundquist¹  | Enikő Lázár¹  | Nan S. Han¹ | Eric B. Emanuelsson²  | Stefan M. Reitzner^{2,3}  | Mark A. Chapman^{2,4} | Vera Shirokova¹ | Kanar Alkass^{1,5}  | Henrik Druid⁵  | Susanne Petri⁶  | Carl J. Sundberg^{2,7}  | Olaf Bergmann^{1,8,9} 

¹Department of Cell and Molecular Biology, Karolinska Institutet, Stockholm, Sweden

²Department of Physiology and Pharmacology, Karolinska Institutet, Stockholm, Sweden

³Department for Women's and Children's Health, Karolinska Institutet, Stockholm, Sweden

⁴Department of Integrated Engineering, University of San Diego, San Diego, USA

⁵Department of Oncology-Pathology, Karolinska Institutet, Stockholm, Sweden

⁶Department of Neurology, Hanover Medical School, Hanover, Germany

⁷Department of Learning, Informatics, Management, and Ethics, Karolinska Institutet, Stockholm, Sweden

⁸Center for Regenerative Therapies Dresden, Technische Universität Dresden, Dresden, Germany

⁹Pharmacology and Toxicology, University Medical Center Göttingen (UMG), Göttingen, Germany

Correspondence

Olaf Bergmann, Department of Cell and Molecular Biology, Karolinska Institutet, Stockholm 17177, Sweden.
Email: olaf.bergmann@ki.se

Funding information

Center for Regenerative Therapies Dresden; Karolinska Institutet; Swedish Research Council; Ragnar Söderberg; Åke Wiberg Foundation; LeDucq Foundation

Abstract

Aim: While manual quantification is still considered the gold standard for skeletal muscle histological analysis, it is time-consuming and prone to investigator bias. To address this challenge, we assembled an automated image analysis pipeline, FiNuTyper (Fiber and Nucleus Typer).

Methods: We integrated recently developed deep learning-based image segmentation methods, optimized for unbiased evaluation of fresh and postmortem human skeletal muscle, and utilized SERCA1 and SERCA2 as type-specific myonucleus and myofiber markers after validating them against the traditional use of MyHC isoforms.

Results: Parameters including cross-sectional area, myonuclei per fiber, myonuclear domain, central myonuclei per fiber, and grouped myofiber ratio were determined in a fiber-type-specific manner, revealing that a large degree of sex- and muscle-related heterogeneity could be detected using the pipeline. Our platform was also tested on pathological muscle tissue (ALS and IBM) and adapted for the detection of other resident cell types (leucocytes, satellite cells, capillary endothelium).

See related editorial: Baltrusch S, 2023. Automated in-depth fiber and nuclei typing in cross-sectional muscle images can pave the way to a better understanding of skeletal muscle diseases. *Acta Physiol.* (Oxf). e14031.

August Lundquist and Enikő Lázár shared first author.

This is an open access article under the terms of the [Creative Commons Attribution-NonCommercial](https://creativecommons.org/licenses/by-nc/4.0/) License, which permits use, distribution and reproduction in any medium, provided the original work is properly cited and is not used for commercial purposes.

© 2023 The Authors. *Acta Physiologica* published by John Wiley & Sons Ltd on behalf of Scandinavian Physiological Society.

Conclusion: In summary, we present an automated image analysis tool for the simultaneous quantification of myofiber and myonuclear types, to characterize the composition and structure of healthy and diseased human skeletal muscle.

KEYWORDS

automated image analysis, myofibers, myonuclei, SERCA, skeletal muscle

1 | INTRODUCTION

Histological analysis of muscle structures is crucial for understanding basic muscle physiology and the tissue's involvement in various pathological conditions. Fundamental research utilizing skeletal muscle histological analysis includes studies on exercise, age-related, and spaceflight-associated changes in the musculature,^{1–8} but also different forms of dystrophies and neuromuscular disorders, such as amyotrophic lateral sclerosis (ALS) and Parkinson's disease.^{9,10} Several automated platforms have been developed to investigate skeletal muscle samples in an unbiased fashion, with the potential to analyze them in a high-throughput format. These approaches allow for the measurement of the size, shape, and type of myofibers in immunohistochemical images^{11–24} (Table S1). Recently, the ability to measure capillarization and model oxygen consumption for individual myofibers¹² and satellite cell identification¹¹ has been added to this toolbox. However, only a few of these automated pipelines allow for simultaneous fiber and myonucleus assignment, based exclusively on the position of the nuclei compared to fiber borders.^{16,20} Routine introduction of myocyte-specific nuclear markers in skeletal muscle histological analysis has been suggested to substantially improve the accuracy and reliability of these types of studies. To date, however, only one such marker has been thoroughly validated in human muscle samples,²⁵ and without the direct assignment of myonuclei to a particular fiber-type population, its usefulness in studying the myofiber–myonucleus relationship is limited.^{5,8,26,27}

Here, we present and validate FiNuTyper, a robust automated platform employing deep learning-based object recognition, for skeletal muscle histological analysis. This novel tool, designed for identifying and quantifying fiber and myonuclear phenotypes, has been optimized for fresh biopsies of healthy and pathological muscle tissue and postmortem samples. In addition, we introduce and validate sarcoplasmic/endoplasmic reticulum calcium ATPase 1 (SERCA1) and 2 (SERCA2) as novel, fiber-type-specific myonuclear markers (Figure 1A). This platform provides a tool for high-throughput histological analysis of the most relevant characteristic of human skeletal muscle in a fiber-type-specific manner, facilitating the

investigation of skeletal muscle biology in homeostasis and disease (Figure 1B).

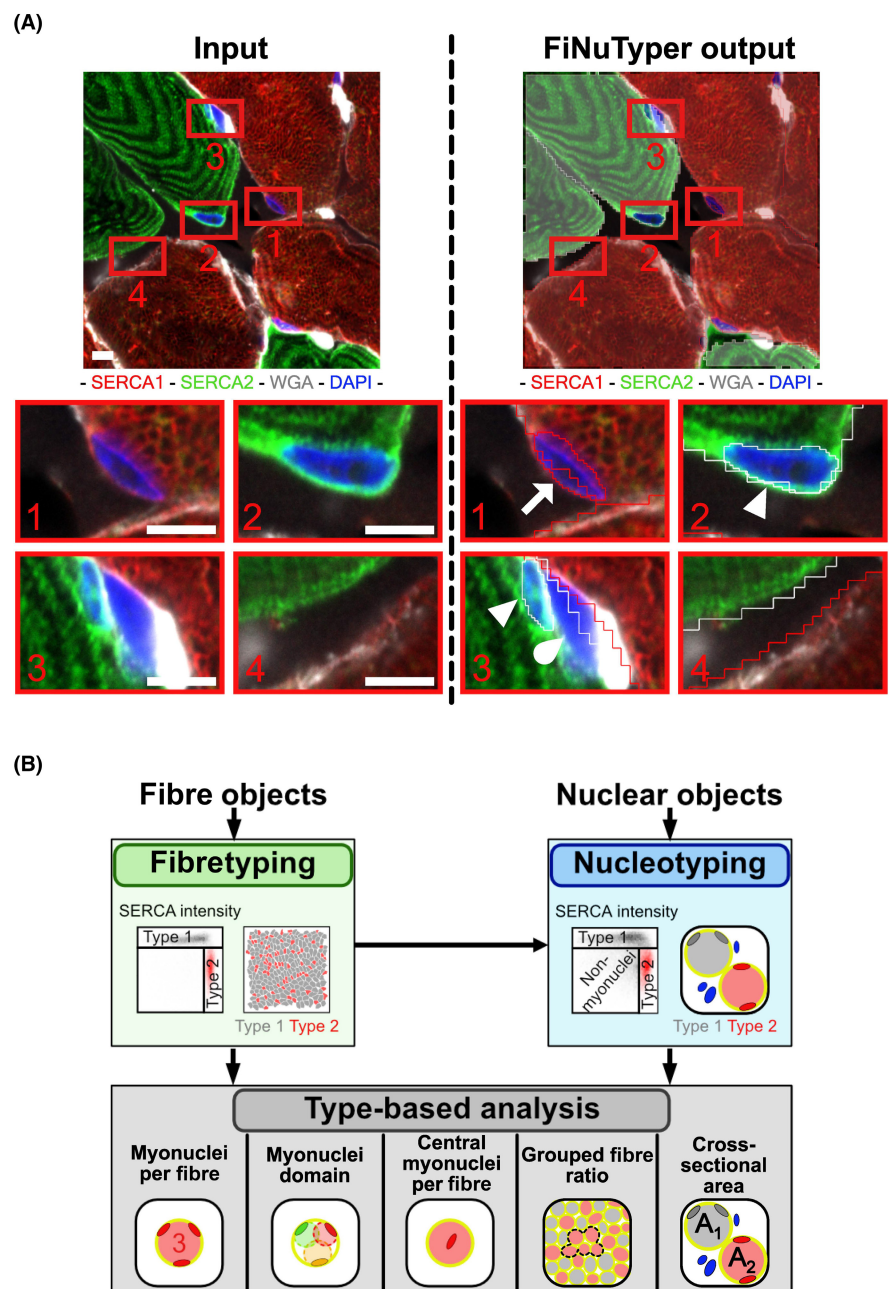
2 | RESULTS

2.1 | SERCA1 and SERCA 2 are fiber-type-specific myonuclear markers

We aimed to establish a simple immunostaining design for the simultaneous, type-specific identification of both myofibers and myonuclei in human skeletal muscle tissue sections, adapted for a classical 4-channel imaging setup available in most fluorescent microscopes. Until now, no myonuclear marker has been described to assign labeled myonuclei to distinct fiber types. Antibodies against slow- and fast-twitch myosin heavy chain isoforms (MyHC1 and MyH2A-2X, respectively), classically used for fiber-type determination in human skeletal muscle studies, do not provide a nuclear or perinuclear signal in myofibers. To overcome this challenge, we investigated the potential use of sarcoplasmic reticulum Ca^{2+} pump proteins SERCA1 and SERCA2 as fast- and slow-twitch myofiber and myonuclear markers in human skeletal muscle, respectively. SERCA1 and SERCA2 have been described to show fiber-type-specific expression patterns, consistent with the MyHC isoform distribution,²⁸ but unlike the fiber-type-specific MyHC contractile proteins, SERCA1 and SERCA 2 are present in a dual, perinuclear, and sarcoplasmic reticulum-related localization, allowing for the identification of both nuclei and fibers of different types in the same section. First, we tested our staining design on transversal sections of postmortem human psoas and pectoralis muscles, combining antibodies against the two SERCA protein isoforms, WGA as cell membrane marker and DAPI as a nuclear stain (Figure 2A). Most fibers, surrounded by a defined WGA signal, were labeled either by SERCA1 or SERCA2 only; however, we also observed fibers simultaneously expressing both SERCA isoforms, suggesting an intermediate phenotype (Figure 2A).

Both SERCA1 and SERCA2 were present in the entire area of the labeled myofibers, in a localization presumably consistent with the position of the sarcoplasmic reticulum (Figure 2B). Moreover, we detected a distinct perinuclear

FIGURE 1 Outline of image processing workflow in FiNuTyper. (A) Input image (left) and graphical output (right) of the analysis performed by FiNuTyper. The areas designated by red rectangles include (1) a SERCA1-positive, type 2 myonucleus (arrow), (2) a SERCA2-positive, type 1 myonucleus (arrowhead), (3) a double negative non-myonucleus (drop) beside a type 1 myonucleus (arrowhead), and (4) an area between fiber borders, not containing any nuclei. The scale bar represents 5 μ m. (B) Overview of the image processing pipeline. Fiber objects, generated in Cellpose²⁹ from the WGA fiber border channel are first typed based on SERCA1 and SERCA2 intensity. Nuclear objects, generated in NucleAIzer³⁰ from the DAPI nuclear channel are typed based on SERCA1 and SERCA2 intensity and corresponding fiber-type adjacency. The typed objects are co-analyzed to produce measurements of myonucleus per fiber, myonuclear domain, central myonucleus per fiber, grouped fiber ratio, and cross-sectional area, separately for each fiber type.



signal with SERCA1 and SERCA2-specific antibodies in the respective myofibers (Figure 2B). We confirmed the close spatial association of this signal with the nuclear membrane, by co-staining with lamin A/C- and SERCA1- or SERCA2-specific antibodies (Figure 2B).

We did not detect any specific SERCA1 or SERCA2 staining in a similar intensity range in non-myocytes outside of the myofiber borders, either in cells dispersed between myocytes (Figure S1A) or more substantial connective tissue borders and vessel walls (Figure S1B), confirming the signal to be highly specific to myofibers and myonuclei. Satellite cells are located between the sarcolemma and basal membrane surrounding myofibers, and as such, could potentially be detected inside the

fiber borders defined by the WGA signal. However, we observed no specific SERCA1 or SERCA2 signal around PAX7-labeled satellite cell nuclei (Figure S1C). Moreover, we performed Western blot analysis with both SERCA1 and SERCA2 antibodies to further confirm the specificity of the used antibodies in human skeletal muscle (Figure S1D).

To assess the relationship between the expression patterns of type 1- or type 2-specific SERCA and MyHC isoforms, we performed co-staining with combinations of MyHC1-, MyHC2A-2X-, and SERCA1- or SERCA2-specific antibodies (Figure 3A) on consecutive tissue sections and plotted the mean signal intensities in three parallel channels, measured in individual fibers (Figure 3B,C). The

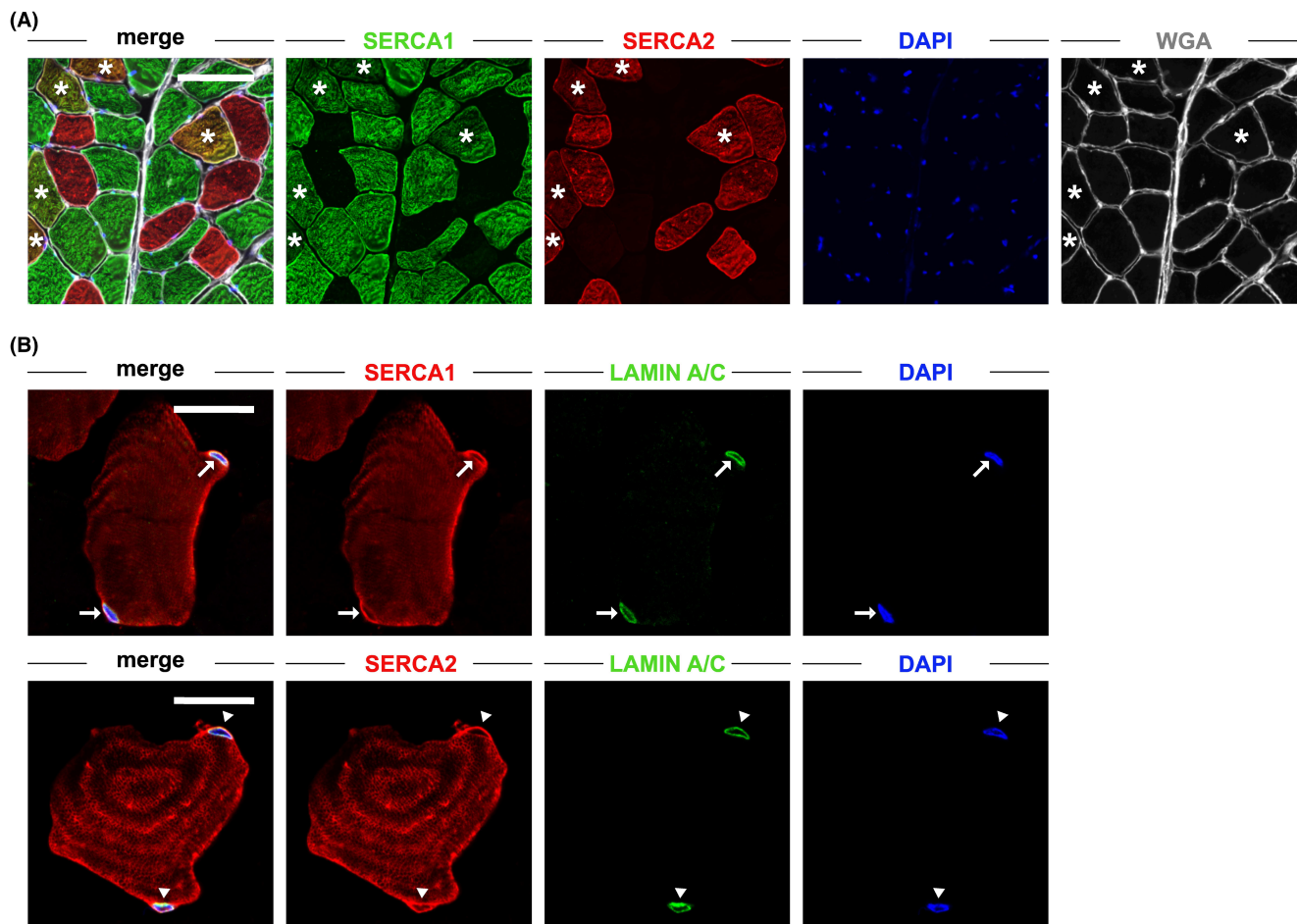


FIGURE 2 SERCA 1 and SERCA2 show distinct perinuclear localization in complementary myofiber populations. (A) Multicolor immunostaining panel using SERCA1 (green) and SERCA2 (red) as myofiber markers, WGA (white) for fiber border, and DAPI (blue) for nuclear labeling, delineate partially overlapping myofiber populations in transversal sections of human skeletal muscle. The selected area contains an exceptionally high number of fibers co-expressing both SERCA isoforms (asterisk). The scale bar represents 100 μ m. (B) SERCA1 and SERCA2 (red) are detected in a distinct perinuclear structure (besides the sarcoplasmic reticulum of the respective fiber type), consistent with the position of the nuclear envelope, showing close spatial association with the nuclear lamina marker lamin A/C. SERCA1-positive myonuclei are marked by arrows, and SERCA2-positive myonuclei are marked by arrowheads. The scale bar represents 20 μ m.

classical fiber-type markers MyHC1 and MyHC2A-2X showed complementary expression patterns with little to no overlap, pointing to a low abundance of hybrid fibers in the analyzed samples (Figure 3A). Most fibers were either co-labeled or not labeled by the combination of the type 2-specific SERCA1 and MyHC2A-2X (Figure 3A,B) and the type 1-specific SERCA2 and MyHC1 antibodies (Figure 3A,C), corroborating the close association between SERCA and MyHC isoform expression. Moreover, we evaluated the reliability of SERCA1 and SERCA2 as fiber-type-specific markers by comparing SERCA-based individual fiber assignment to type 1 and type 2 populations to that based on the MyHC isoform expression pattern, currently considered the gold standard of fiber-type analyses (Figure 3D,E). Based on the dataset collected from post-mortem psoas tissue of three subjects covering a wide age range (25, 45, and 73 years) and a stringent gating strategy

based on the position of a clearly defined double-positive fiber population, we found both SERCA1 and SERCA2 to be highly sensitive ($99.71 \pm 0.30\%$ and $100 \pm 0.00\%$, mean \pm SD, respectively) and specific ($98.77 \pm 1.35\%$ and $98.91 \pm 1.21\%$, mean \pm SD, respectively) markers of type 2 and type 1 myofibers (Figure 3F), independent from the age of the individual.

2.2 | FiNuTyper quantifies skeletal muscle microscopy images with high accuracy

After confirming that the sarcoplasmic reticulum- and nuclear envelope-associated SERCA1 and SERCA2 signals allow for simultaneous myofiber- and nucleotyping, we designed a simple immunostaining panel to stain

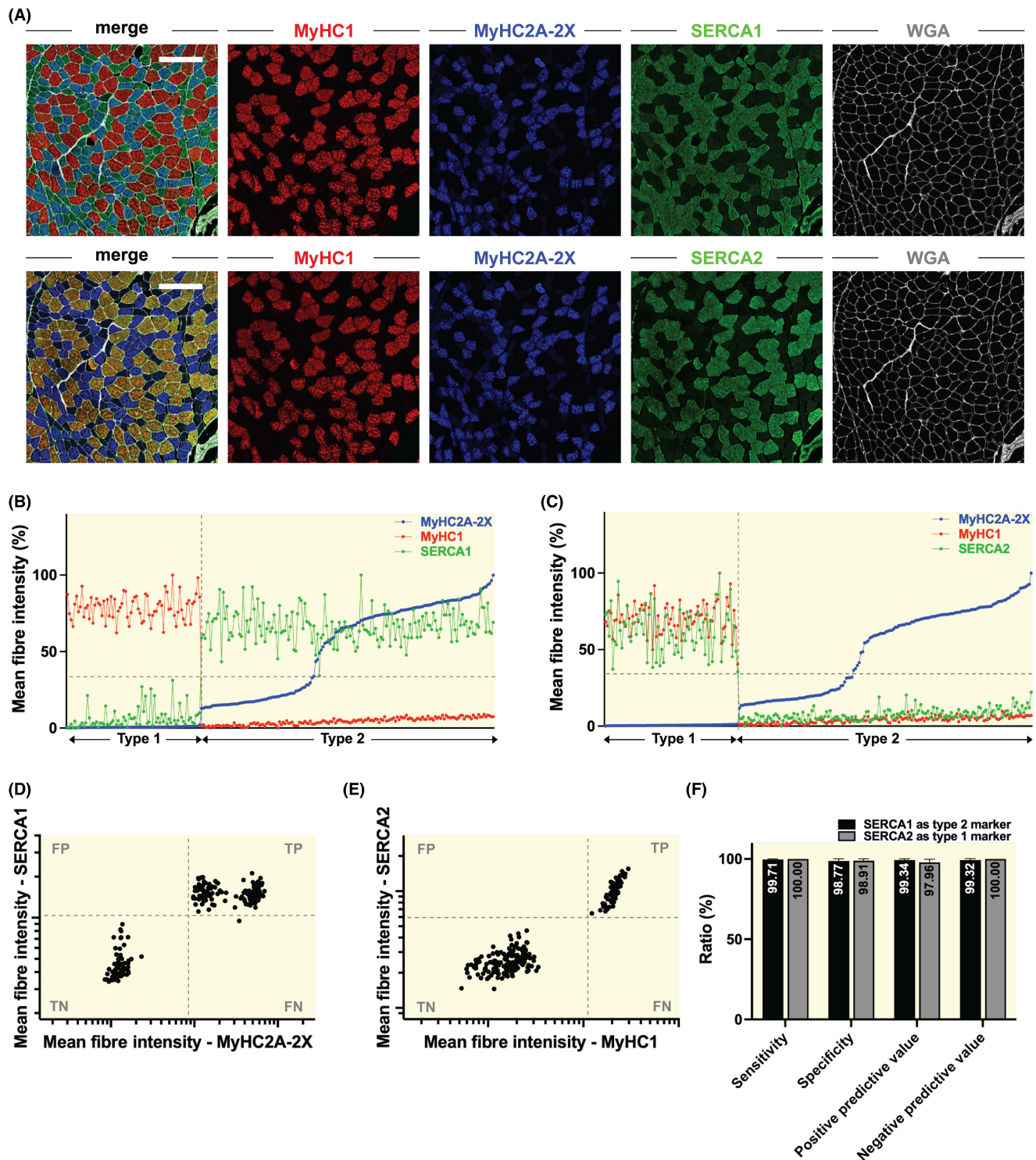


FIGURE 3 SERCA- and MyHC-based fiber-typing approaches provide consistent results in human skeletal muscle. (A) Co-staining of a transversal section of human skeletal muscle with antibodies against classical myosin heavy chain markers and the two SERCA isoforms confirm almost complete overlap between SERCA1 (upper panel, green) and MyHC2A-2X (blue), as well as SERCA2 (lower panel, green) with MyHC1 (red) labeling. The scale bar represents 200 μ m. (B) Mean signal intensity distribution of SERCA1 (green) and (C) SERCA2 (green) align with type 2 and type 1 fiber identities, assigned based on MyHC2A-2X (blue) and MyHC1 (red) mean signal intensities measured in individual myofibers of the same area (single scans, $n = 236$ fibers). (D) The gating strategy to compare corresponding MyHC- and SERCA isoform-based fiber type assignment for type 2 and (E) type 1 myofibers uses stringent cutoffs, based on the signal intensities of the defined double-positive populations. TP, true positives (SERCA⁺-MyHC⁺); FP, false positives (SERCA⁺-MyHC⁻); FN, false negatives: (SERCA⁻-MyHC⁺); true negatives: SERCA⁻-MyHC⁻. (F) Sensitivity, specificity, positive and negative predictive values of SERCA1 as a type 2 (black columns) and SERCA2 as a type 1 (gray columns) myofiber marker (based on $n = 3$ subjects, 3 image scans/subject, mean \pm SD).

transversal sections of human skeletal muscle, using antibodies against the two SERCA isoforms, combined with fluorescently conjugated WGA as cell membrane marker and DAPI as a nuclear stain (Figure 1A). Confocal microscopy images, captured from sections processed with this panel, were submitted to FiNuTyper, our automated image analysis pipeline, built on the recently reported image segmentation tools CellPose²⁹ and NucleAIzer.³⁰

Since the primary output of any fiber- or nucleotyping approach is the number of identified objects and fiber cross-sectional area values, we sought to benchmark our automated tool against manual evaluation, by deriving these parameters from the same image sets and comparing the obtained results.

We assessed the accuracy of FiNuTyper-based fiber (Figure 4A) and myonuclear identification (Figure 4B)

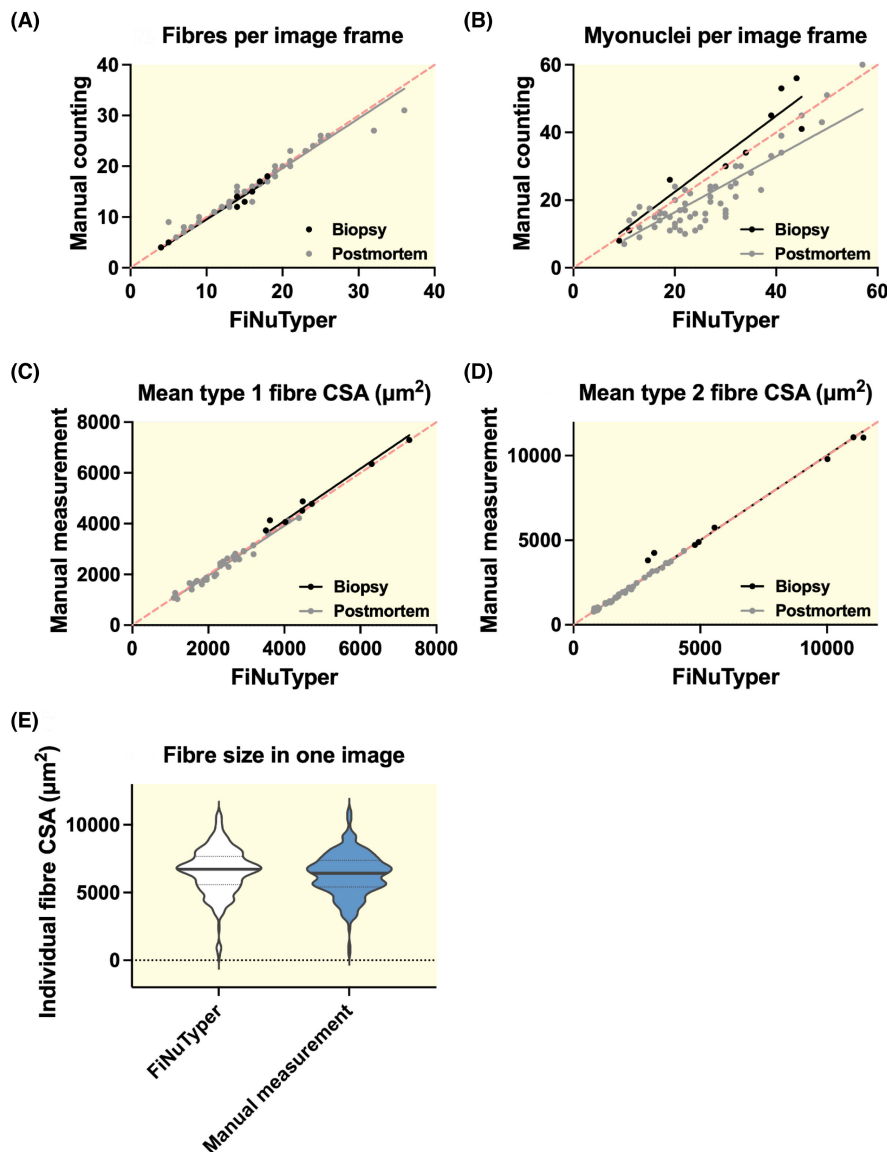


FIGURE 4 Automated SERCA-based image analysis by FiNuTyper provides results comparable to the manual evaluation of human skeletal muscle sections. (A) Comparison of the number of fibers per-image frame (ICC = 0.985 (0.923–0.997), $n = 9$ for fresh biopsies (black); ICC = 0.977 (0.962–0.987), $n = 57$ for postmortem tissue, (gray)); (B) number of myonuclei per-image frame (ICC = 0.912 (0.641–0.980), $n = 9$ for fresh biopsies (black); ICC = 0.790 (0.268–0.918), $n = 57$ for postmortem tissue, (gray)); (C) type 1 fiber cross-sectional area per-image frame (ICC = 0.988 (0.947–0.998), $n = 9$ for fresh biopsies, (black); ICC = 0.997 (0.990–0.999), $n = 35$ for postmortem tissue, (gray)) and (D) type 2 fiber cross-sectional area per-image frame (ICC = 0.982 (0.855–0.997), $n = 9$ for fresh biopsies (black); ICC = 0.985 (0.969–0.993), $n = 35$ for postmortem tissue (gray)), determined manually and generated by the automated approach. Linear regression lines were forced to intersect $x, y = 0, 0$. The line of identity is displayed in red. The image frame size was approximately $0.3 \times 0.3 \text{ mm}^2$. ICC: intraclass correlation coefficient, single measure (95% confidence interval). (E) Fiber size distribution in a single image scan (approximately $0.9 \times 0.9 \text{ mm}^2$) based on automated ($n = 243$, white) and manual ($n = 254$, blue) evaluation.

on frozen sections of fresh vastus lateralis muscle and postmortem psoas major and pectoralis major muscle, by calculating intraclass correlation coefficients (ICC, 95% CI) between the output values of the manual and automated analyses. FiNuTyper displayed an ICC of 0.977 (0.962–0.987) for fiber identification in the postmortem and 0.985 (0.923–0.997) in the fresh biopsy image sets, confirming an “excellent” agreement between the two independent approaches according to ICC reporting guidelines³¹ (Figure 4A). The high level of accordance between FiNuTyper-based and manual evaluation was also upheld when performing myonuclear identification in the bioptic samples, with an ICC of 0.912 (0.641–0.980) (Figure 4B). While still showing a “good” overall correlation, we obtained more variable results in the postmortem dataset with an ICC of 0.790 (0.268–0.918) (Figure 4B). This is likely due to different postmortem intervals and thus, varying tissue quality of the analyzed samples, which seems to have a more pronounced effect on the reliability of nucleotyping than of fibertyping.

Since type 1 and type 2 fibers often respond to physiological and pathological challenges by changing their sizes and shapes differently, we decided to validate the automated fiber cross-sectional area (CSA) determination by FiNuTyper (Figure 4C,D) on a fiber-type basis in both postmortem and fresh bioptic samples, against manual measurements. Our analysis revealed a very strong correlation between the manually collected and automatically generated mean CSA values, independent of the fiber type or source of the tissue sample (ICC of type 1 fiber CSA measurements in postmortem tissue: 0.997 (0.990–0.999) and in bioptic tissue: 0.988 (0.947–0.998); ICC of type 2 fiber CSA measurements in postmortem tissue: 0.985 (0.969–0.993) and in bioptic tissue: 0.982 (0.855–0.997)). We performed Bland–Altman analysis on the validation dataset and displayed the results along with the 95% limit of agreement values (Figure S2A–D). We also evaluated the cross-sectional area at the level of individual fibers within a single image scan and found a highly similar fiber size distribution between the manual and automated output (Figure 4E), further confirming the reliability of CSA measurements performed by FiNuTyper.

2.3 | Sex, muscle, and fiber type determine myocyte and myonuclear characteristics

To demonstrate the advantages of FiNuTyper in the analysis of larger image sets, we processed paired samples of postmortem psoas major and pectoralis major muscles of five male and five female individuals, deceased between 44 and 55 years of age, and submitted three image scans (9

stitched frames, approx. $0.9 \times 0.9 \text{ mm}^2$) taken from distinct areas of each muscle sample to the automated pipeline. In total, we identified and analyzed approximately 15 600 (780.5 ± 70.7 per muscle sample, mean \pm SD) muscle fibers and 12 500 (625.4 ± 46.3 per muscle sample, mean \pm SD) myonuclei in the processed image scans.

In results compiled from both sexes, we found type 1 fibers in significantly higher proportion in the psoas than in the corresponding pectoralis samples (Figure 5A, $p=0.0079$), corroborating the postural function of the psoas muscle in contrast to the more dynamic movement profile supported by the pectoralis muscle. The fiber-type-specific difference between the two tissues, however, disappeared on the myonuclear level (Figure 5B). This suggests that type 1 fibers on average contribute more to the myonuclear pool than type 2 fibers, explaining the discrepancy between fiber and myonuclear ratios in the psoas and pectoralis muscles.

FiNuTyper allows for the identification of grouped fibers, here defined as myofibers having three or more direct neighbors of the same type.³² This value varied most in the functionally dominant psoas type 1 and pectoralis type 2 fibers, with the latter showing a significantly higher grouped fiber ratio compared to type 1 fibers in the same muscle (Figure 5C, $p=0.0025$). Some of this difference, however, is due to the distinct fiber-type composition of the two studied muscles.³³ Further mathematical analysis, aiming to minimize the intrinsic bias caused by the unequal abundance of the studied fiber subsets, can benefit from information on fiber-type distribution, and other geometric parameters such as cross-sectional area, readily available for every single fiber after the automated analysis.

The relationship between type 1 and type 2 fiber cross-sectional areas largely depends on the prevalent function of most muscles. Accordingly, in our pooled dataset type 1 fibers displayed a larger CSA than type 2 fibers in the psoas major, supporting its postural role (Figure 5D, $p=0.0001$). In the pectoralis with a more dynamic function, we found no significant difference in size between the two fiber types, explained by the type 2 fibers being almost twice as large as their counterparts in the psoas (Figure 5D, $p=0.0184$). Males manifested strikingly larger CSA values in all four studied fiber subsets compared to females (Figure 5D). The relationship between data points collected from the same individual was largely similar over the entire dataset and between sexes, except for the CSA of pectoralis type 2 fibers, which seemed to follow distinct trends in males and females. While in males these fibers were as large as pectoralis type 1 fibers (Figure 5E) and almost twice as big as psoas type 2 fibers (Figure 5D), in females they showed the opposite pattern, being significantly smaller

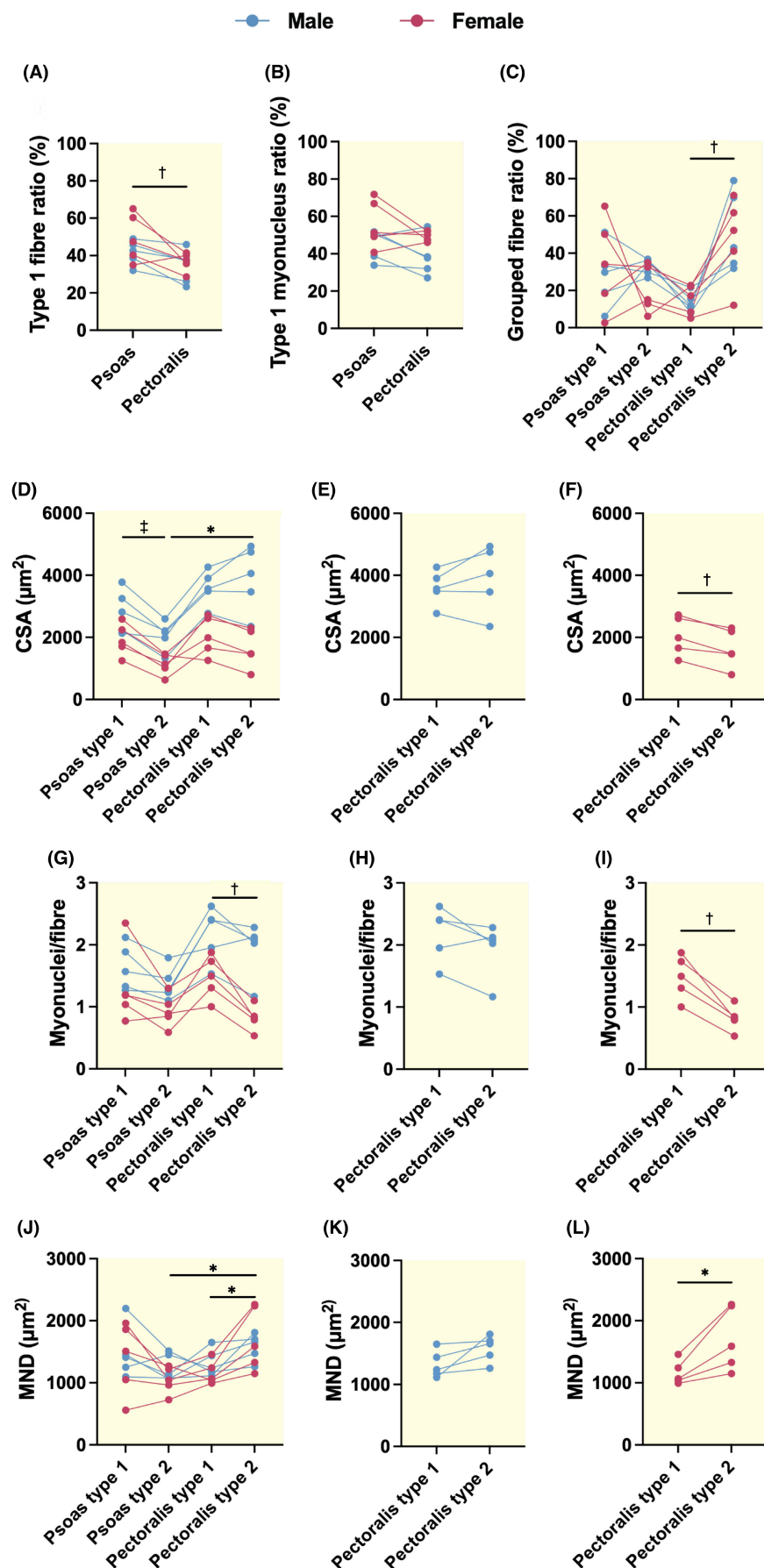


FIGURE 5 FiNuTyper identifies sex-, muscle- and fiber type-specific characteristics in healthy human skeletal muscle. Fiber- and myonuclear evaluation of healthy skeletal muscle tissue was performed by the FiNuTyper pipeline. Data was collected and pooled from 3, approx. $0.9 \times 0.9 \mu\text{m}^2$ image scans of postmortem psoas major and pectoralis major samples of five males (blue data points) and five females (orange data points) between 44–55 years of age. Data points derived from the same subject are visualized with a connecting line. (A) Type 1 fiber and (B) myonucleus ratios of psoas and pectoralis muscle. (C) Grouped fiber ratios of type 1 and type 2 fibers in the psoas and pectoralis muscle. (D) Cross-sectional area (CSA) of type 1 and 2 fibers in the psoas and pectoralis muscle. (E) Analysis of paired male and (F) female CSA data points in pectoralis type 1 and type 2 fibers. (G) Myonucleus per fiber values of type 1 and 2 fibers in the psoas and pectoralis muscle. (H) Analysis of paired male and (I) female data points in pectoralis type 1 and type 2 fibers. (J) Myonuclear domain size (MND) of type 1 and 2 fibers in the psoas and pectoralis muscle. (K) Analysis of paired male and (L) female data points in pectoralis type 1 and type 2 fibers. Statistical analysis was performed between all compared datasets, with one-way ANOVA and Tukey post hoc test (C, D, G, J), paired *t* tests (A, B, E, F, I, K, L), or Wilcoxon matched-pairs signed rank test (H), depending on the results of previous normality test. Statistical significance was set to $p < 0.05$ and marked with an asterisk (* $p < 0.05$; † $p \leq 0.01$; ‡ $p \leq 0.001$; lack of statistical difference was not marked on the plots).

than the type 1 fibers of the same muscle (Figure 5F, $p=0.0037$) and in the same size range as their counterparts in the psoas major (Figure 5D).

We observed a similar trend to the CSA measurements in the myonuclei per fiber values between psoas type 1 and type 2 fibers (Figure 5G). On the other hand, we found a pronouncedly higher myonuclear content in type 1 than in type 2 fibers of the pectoralis muscle (Figure 5G, $p=0.0082$), in contrast to their similar CSA values. When analyzing the data points of the two sexes separately, this difference disappeared in the male cohort (Figure 5H), while the female pectoralis type 1 and type 2 fibers exhibited a similar relationship as in the pooled dataset (Figure 5I, $p=0.0031$). These results corresponded well with the distinct pattern of CSA values seen in the male and female pectoralis muscles (Figure 5E,F).

Based on the classical concept of the myonuclear domain (MND), the number of myonuclei assigned to single fibers should follow changes in the CSA, however, this assumption has been challenged in recent years.^{26,34,35} We calculated the MND for all four fiber subsets in each subject (Figure 5J). Pectoralis type 2 fibers on average showed higher MND compared to both psoas type 2 (Figure 5J, $p=0.0289$) and pectoralis type 1 fibers (Figure 5J, $p=0.0161$). The latter difference, however, was not present separately in the male cohort (Figure 5K) and was driven by two female subjects (Figure 5L, $p=0.0244$), who also had the largest MND in psoas type 1 fibers in the female cohort (Figure 5J).

All these results indicate sex-specific mechanisms and the relevance of individual-based factors in determining fiber-type characteristics of different muscles (Figure 5A–L). The mean values and standard deviation of all assessed parameters, calculated in the pooled cohort and male and female subjects separately, are displayed in Table S2.

2.4 | Automated SERCA-based muscle analysis reveals pathological changes in ALS and IBM

To test the applicability of the FiNuTyper pipeline to pathological muscle tissue, we analyzed vastus lateralis muscle biopsies from two female donors with amyotrophic lateral sclerosis (ALS), and a male patient with inclusion body myositis (IBM). First, we examined whether the association between corresponding SERCA and MyHC isoforms, observed in healthy tissue, remains intact in a tissue severely affected by ALS. We compared MyHC1-MyHC2A-2X- and SERCA1-SERCA2-specific labeling in identical areas of consecutive tissue sections and found almost complete accordance between the signal patterns acquired from the two parallel stainings (Figure 6A), suggesting

that SERCA1 and SERCA2 detection allows for fiber-type discrimination even under pathological conditions.

For the detailed analysis of the pathological muscle samples, we compiled data from two (ALS #2 subject, 64 fibers and 281 myonuclei analyzed; IBM #1 subject, 68 fibers and 192 myonuclei analyzed) or three (ALS #1 subject, 306 fibers and 567 nuclei analyzed) image scans (approx. $0.9 \times 0.9 \text{ mm}^2$) and compared the results to sex-specific reference values of fiber-type composition and cross-sectional area, determined by a meta-analysis of 19 independent studies, focusing on subject above 40 years of age (Figure 6B–D).³⁶

The first donor (ALS #1, female, 50 years of age) suffered from end-stage ALS with a bulbar onset for 8 years, and accordingly, we observed severe alterations of the muscle architecture with thickened connective tissue walls between muscle cells and pronounced atrophy and loss of type 2 myofibers (Figure 6B, first and second panels). As expected, the most severely damaged type 2 fiber remnants were not identified as individual fiber objects by the pipeline, with the few annotated type 2 fibers retaining the most resemblance to the normal fiber phenotype (Figure 6B, first and second panels). The extremely high ratio of type 1 fibers (99.4%), in comparison with the balanced distribution of fiber types according to the healthy reference value ($48.1 \pm 2.6\%$, mean \pm SD), supported our initial finding of substantial type 2 fiber loss in the diseased sample (Figure 6B, third panel). At the same time, CSA of type 1 fibers in the ALS sample ($4659 \mu\text{m}^2$) was above the published reference range ($3829 \pm 180 \mu\text{m}^2$, mean \pm SD) (Figure 6B, fourth panel), indicating a hypertrophic response in this fiber population.

In case of the second donor (ALS #2, female, 71 years of age), we did not observe signs of similar fiber atrophy or selective loss of a fiber type. On the contrary, all identified fibers appeared to be massively enlarged (Figure 6C, first and second panels). The ratio of type 1 fibers (31.25%) was lower than the reference value (48.1 ± 2.6 , mean \pm SD; Figure 6C, third panel), which could be explained by fiber-type clustering dominated by type 2 fibers, previously described in ALS.³⁷ The average CSA for type 1 fibers ($7292 \mu\text{m}^2$; Figure 6C, fourth panel) was approximately twice, and for type 2 fibers ($11\,728 \mu\text{m}^2$; Figure 6C, fifth panel) approximately 4.5 times as large as the reference values ($3829 \pm 180 \mu\text{m}^2$ and $2652 \pm 196 \mu\text{m}^2$, mean \pm SD, respectively), demonstrating hypertrophy of the fibers. Notably, the type 2 fibers were on average larger than the type 1 fibers, as opposed to the reference values.

The third donor (IBM #1, male, 69 years of age) suffered from inclusion body myositis, an inflammatory myopathy characterized by the presence of so-called inclusion bodies inside, and substantial leucocyte infiltration between the muscle fibers. In this sample, we also

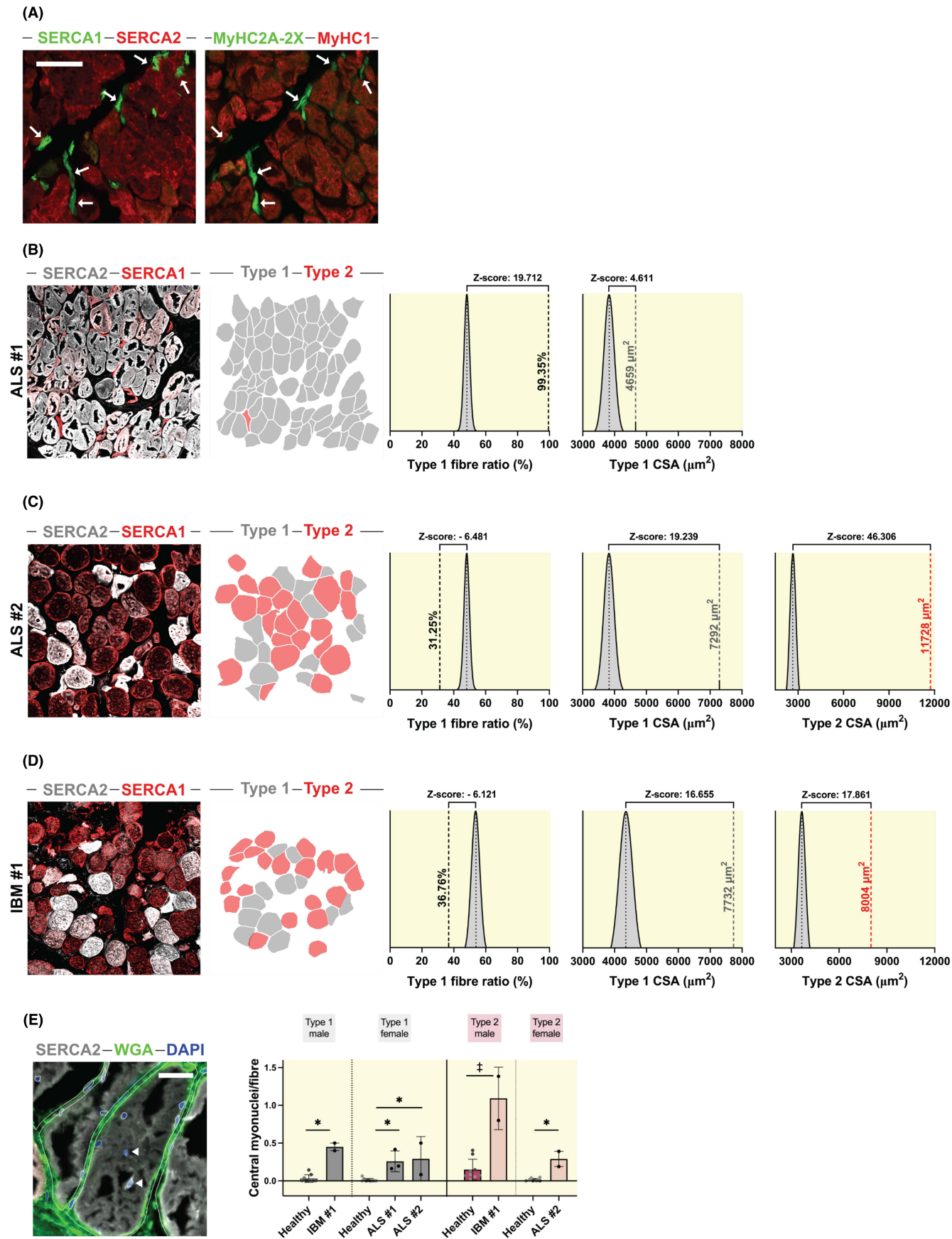


FIGURE 6 FiNuTyper detects pathology-related changes in muscle affected by ALS and IBM. (A) SERCA1 (green) – SERCA2 (red) (left panel) and MyHC2A-2X (green) – MyHC1 (red) (right panel) labeling provides highly similar staining patterns in consecutive sections of skeletal muscle tissue of an ALS patient. Type 2 fibers identified by SERCA1 or MyHC2A-2X expression are marked by arrows. The scale bar represents 100 μm . (B, C) Analysis of vastus lateralis muscle biopsy of two ALS patients, and (D) an IBM patient. SERCA2 (white) and SERCA1 (red) immunostaining signal (first panels) provides the input for the segmentation of type 1 (gray) and type 2 (red) fibers (second panels). Type 1 fiber ratio (%; third panels), mean type 1 fiber CSA (μm^2 , fourth panels), and mean type 2 fiber CSA (μm^2 , fifth panels) were calculated from pooled data of two or three, approx. $0.9 \times 0.9 \mu\text{m}^2$ image scans ($n = 307, 64$, and 68 identified fibers per case, respectively) per subject. Z-scores were calculated in comparison with reference values of healthy male and female vastus lateralis tissues,³⁶ assuming normal distribution of the reference data. (E) Centrally located myonuclei (arrowheads) are more frequent in both fiber types of the pathological tissue samples (light black and light red bars) than in the pectoralis major of three healthy, sex-matched subjects (dark gray and dark red bars). Two or three, $0.9 \times 0.9 \mu\text{m}^2$ image scans per subject were analyzed and treated as technical replicates for comparison. Statistical analysis was performed between three groups with one-way anova and post hoc Dunnett's test. Comparison of two groups was performed with *t* test or Mann-Whitney *U* test, and the statistical significance was set to $p < 0.05$ and marked with an asterisk (*: $p < 0.05$; † $p \leq 0.01$; ‡ $p \leq 0.001$). The scale bar represents 40 μm .

observed an increased fiber size (Figure 6D, first and second panels), in line with studies describing the frequent occurrence of fiber hypertrophy in muscles of the affected individuals.^{38,39} Similar to the ALS #2 case, we detected a lower proportion of type 1 fibers in this sample (36.76%; Figure 6D, third panel) compared with the reference value ($53.9 \pm 2.8\%$, mean \pm SD). We found the average CSA for type 1 ($7732 \mu\text{m}^2$; Figure 6D, fourth panel) and type 2 ($8004 \mu\text{m}^2$; Figure 6D, fifth panel) fibers in a similar range, pointing at a general hypertrophic response in comparison with normal reference values ($4352 \pm 203 \mu\text{m}^2$ and $3628 \pm 245 \mu\text{m}^2$, mean \pm SD, respectively).

Muscle damage often initiates regenerative processes in the affected tissues with a common manifestation of increased frequency of centrally located myonuclei (Figure 6E), signaling ongoing myonuclear accretion to the impaired fibers. We compared the number of centrally located myonuclei per fiber in two (ALS #2 and IBM #1) or three (ALS #1) technical replicate image scans of the pathological biopsies to three healthy female and three healthy male pectoralis samples in our postmortem dataset and found significantly higher values in the diseased samples in both fiber types (Figure 6E). All these observations are in line with our current understanding of ALS and IBM disease progression in human skeletal muscle and confirm that the FiNuTyper pipeline is adept at detecting pathology-related phenomena when analyzing diseased skeletal muscle tissue.

3 | DISCUSSION

Despite numerous technological advancements of late, immunohistochemical analysis of bioptic samples remains the methodological touchstone of skeletal muscle research. Acknowledging the importance of this approach, a substantial number of automated tools have been presented in recent years (Table S1), aiming to increase the speed, accuracy, and extent of the microscopic

image evaluation and avoid operator-induced bias, the most obvious limitations of the classical manual quantification. Each of these algorithms assesses biologically relevant myofiber characteristics, however, only a few of them perform simultaneous myonucleus assignment, relying exclusively on positional cues of nuclear objects in relation to the sarcolemma.^{16,20} Challenges of unequivocal myonucleus identification have been pointed out as a major source of controversies around cellular processes involving myonuclear accretion or apoptosis.⁵

With FiNuTyper, we present the first automated image analysis pipeline utilizing myonuclear markers for skeletal muscle immunohistological evaluation. The only previously reported myonuclear marker, pericentriolar material 1 (PCM-1),²⁵ which is a component of the perinuclear matrix in mature myonuclei, does not allow for direct fiber-type assignment.²⁵ We used SERCA1- and SERCA2-specific immunostaining to obtain a distinct perinuclear signal on top of the extensive sarcoplasmic reticulum labeling in type 2 and type 1 myofibers, respectively. This approach holds the additional advantage of allowing for simultaneous fiber- and myonucleotyping in the same muscle section.

We performed meticulous validation of the SERCA1- and SERCA2-specific antibodies used in our study. We found no specific SERCA2 labeling in an intensity range similar to that in muscle fibers in any other muscle-resident cell type, although the SERCA2b isoform has been reported to have a ubiquitous expression.²⁸

We performed detailed characterization of MyHC and SERCA isoform expression patterns in various healthy muscle samples and in pathological tissue. We found a high degree of concordance between the two labeling strategies, even in older individuals, where it has been suggested that the coordination between SERCA and MyHC isoforms might break down.³³ Notably, in several samples, we detected a subpopulation of SERCA2-positive fibers with an intermediate level of SERCA1 expression (Figure S3A,B). A higher variability

in SERCA isoform expression in muscle fibers has been reported in response to certain physiological and pathological stimuli.^{40–43} These observations attest to a significantly larger phenotypic range of muscle fibers than what the classical, MyHC isoform-based type 1-type 2 categories can account for, which can be an interesting focus of future research.

FiNuTyper utilizes a combination of deep learning-based approaches for automated image analysis, allowing for fast, and highly accurate identification and characterization of fiber and myonuclear objects in human skeletal muscle tissue under various experimental conditions. Concerning accuracy performance, we found the quality of tissue and staining in the analyzed image play the largest roles. In our hands, the integrity and conciseness of the fiber border are the most significant contributors to this type of quality difference. Since the quality of tissue is difficult to control for, and there is some confusion regarding how to quantify methodological reliability within the field,⁴⁴ we refrain from directly comparing the accuracy of FiNuTyper to other published automated approaches. However, the most obvious advantage of our approach is the embedded machine learning algorithms Cellpose and NucleAIzer, which achieve superior identification of cell nuclei and cell borders compared to other non-machine learning-based strategies^{29,30} implemented in most other automated approaches (Table S1). The accuracy of myonuclear identification by FiNuTyper, compared to manual evaluation, is still considered good to excellent according to convention.³¹ This is also, however, the feature most affected by poor tissue quality, underlining the technical difficulties in this type of analysis when solely relying on the localization of myonuclei inside of the sarcolemma border. A high level of object recognition fidelity is required for proper fiber shape retention in the small peripheral region where the myonuclei are located, and only a few pixels of error in the identified fiber area might give rise to a neighboring cell's nucleus appearing within the fiber border and thus being considered a myonucleus. By including SERCA1 and SERCA2 as specific myonuclear labels in our staining panel, in addition to evaluating the spatial proximity between the nuclei and the sarcolemma, we established a stringent, dual filtering strategy for myonuclear identification, which provides reliable results, even in challenging samples.

We showcased the overall efficiency and robustness of FiNuTyper-based evaluation by analyzing postmortem muscle samples of five male and five female subjects from the same age group (44–55 years). We collected tissue from two different muscles of the deceased donors, the psoas major and the pectoralis major, that is either inaccessible or rarely sampled in studies using biopsies from

living subjects. This allowed us to evaluate myocyte- and myonucleus-related parameters at the level of the individual, muscle source (psoas major and pectoralis major), and fiber type (type 1 or type 2).

Moreover, we performed automated analysis on muscle biopsies of two patients suffering from amyotrophic lateral sclerosis and another individual suffering from inclusion body myositis. Our results demonstrated that FiNuTyper, beyond characteristics of healthy muscle tissue, also successfully identifies features associated with muscle pathologies and regenerative processes, such as the loss of fast-twitch motor units, fiber hypertrophy, and a high frequency of centrally located myonuclei.^{45–48}

The versatility of FiNuTyper relies largely on the Cellprofiler environment,^{49,50} which allows for various adaptations of the original pipeline to answer other relevant research questions in the skeletal muscle field. To demonstrate this, we supply five additional annotated pipelines that build on the same basic principles but produce different outputs or utilize different markers. These include identifying and quantifying the hybrid myofiber and myonuclear populations using the SERCA markers (Figure 7A), capillarization on a fiber-type basis using UEA I, satellite cells using PAX7, tissue-resident and infiltrating immune cells using CD45 (Figure 7B), and fiber typing based on conventional MyHC markers. Validating these pipelines is beyond the scope of this project, but we supply them, along with example images, as stepping-stones for further research (Files S1, S2 and S3 are provided as Mendeley data DOI: [10.17632/dfw8r794ph.3](https://doi.org/10.17632/dfw8r794ph.3)). Another strength of FiNuTyper is its applicability with different microscopes and imaging settings. Without any modification to the original workflow, we obtained similar results on images captured with an epifluorescent microscope and with our standard confocal setup (Figure S4), supporting the platform's suitability to routine clinical diagnostic use.

To conclude, with FiNuTyper we present an automated method for the high-throughput evaluation of the most important aspects of skeletal muscle histology, including simultaneous myofiber and myonucleus type analysis. For this goal, we have introduced and validated SERCA1 and SERCA2 as a novel, type 2- and type 1-specific myofiber and myonuclear markers, respectively. We have shown that our pipeline delivers results in line with human manual evaluation and is robust enough to discern sex-, muscle origin-, and fiber-type-specific differences even in a relatively small sample population. The platform can also be successfully applied to pathological muscle samples, is applicable in various imaging settings, and is highly customizable, which we demonstrate by providing five additional pipelines for the analysis of other resident cell types, capillaries, and hybrid myofibers. FiNuTyper

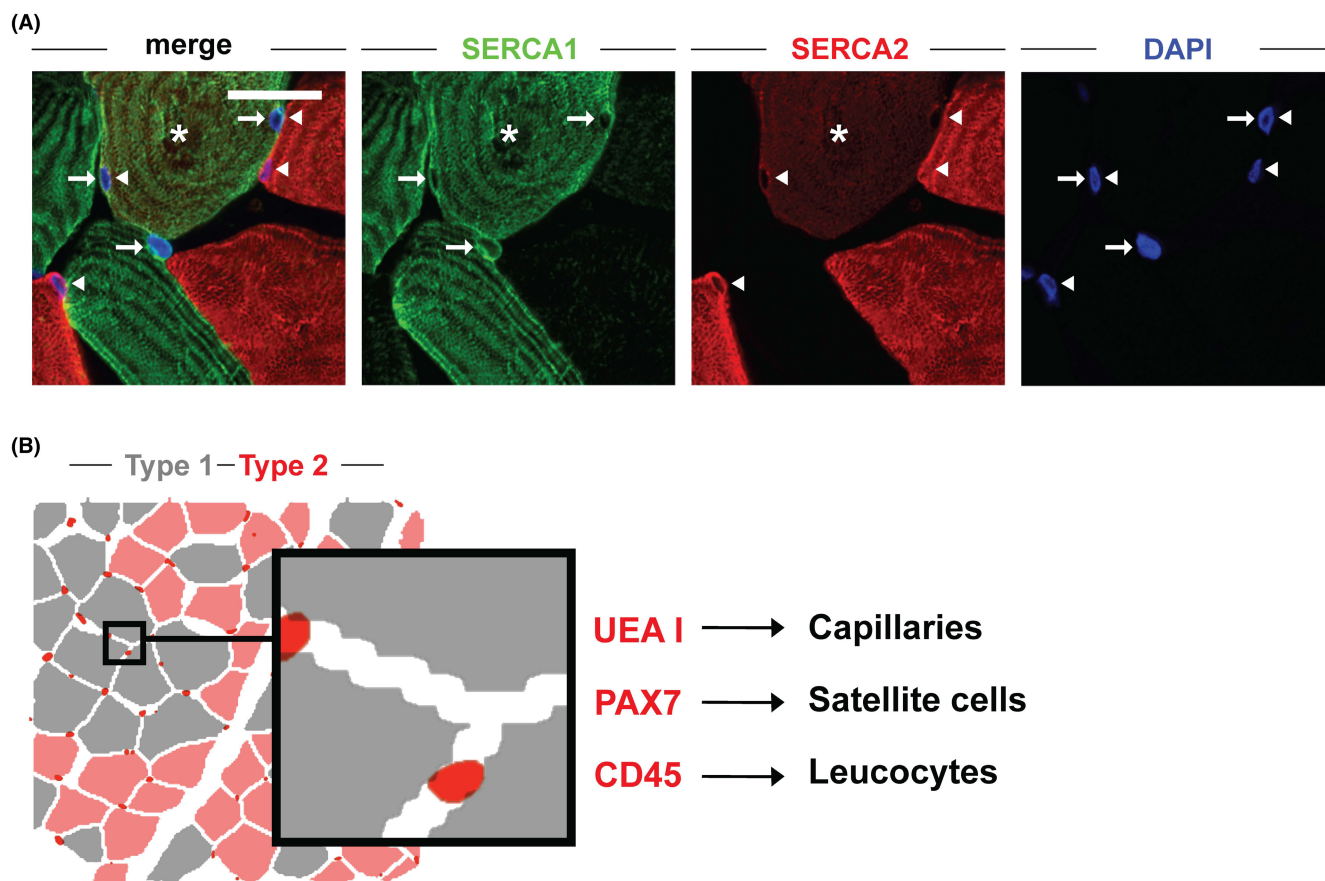


FIGURE 7 Versatility of FiNuTyper in other experimental settings. (A) Quantification of hybrid myofibers (asterisk) is based on the co-expression of the two SERCA isoforms, which also allows for the identification of hybrid myonuclei with overlapping perinuclear SERCA1 (arrow) and SERCA2 (arrowhead) signals. (B) Schematic overview of modified FiNuTyper applications includes capillary identification based on UEA I labeling, satellite cell identification based on nuclear PAX7 expression, and immune cell identification based on the presence of the CD45 marker.

requires little technical knowledge and no coding skills to run or modify it. Together, FiNuTyper facilitates batch-processing of large image sets and analysis of multiple muscle characteristics, while increasing robustness and reproducibility in image-based skeletal muscle research.

4 | METHODS

4.1 | Study subjects, tissue collection, and ethics

Postmortem tissue samples of psoas major and pectoralis major muscles were collected at the Department of Oncology-Pathology of Karolinska Institutet, Sweden, from 21 overall healthy donors during routine autopsies, with the informed consent of relatives (ethical permit number: Dnr 02-418.) Tissue biopsies from the vastus lateralis muscle of one IBM and two ALS patients were provided by Susanne Petri from Hannover Medical School, Germany (ethical permit number: 6269). Tissue sections

and total cell lysates of vastus lateralis muscle biopsies, collected from 7 healthy subjects, were provided by Carl Johan Sundberg from Karolinska Institute, Sweden (ethical permit number: Dnr 2016/590-31). Sex, age, and sampled muscles of the study subjects are listed in Table S3, while a summary of figures and datasets in which images or data from particular study subjects were included is presented in Table S4. Sex was assigned based on the entry into the population register and following external and internal examination of body characteristics in postmortem cases. Bioptic cases were assigned based on patient self-report.

4.2 | Tissue handling and cryosectioning

The postmortem muscle samples and the tissue from the ALS and IBM subjects were cut into approximately $5 \times 5 \times 5 \text{ mm}^3$ segments and then placed in a cryomold filled with Tissue-Tek O.C.T Compound (Sakura), in an orientation allowing for transversal sectioning of the

myofibers. The tissue blocks were flash-frozen in an isopentane-dry ice slurry, while the fresh biptic muscle samples were flash-frozen in liquid nitrogen-cooled isopentane, and then stored at -80°C until sectioning. $5\mu\text{m}$ (postmortem tissue for imaging controls), $7\mu\text{m}$ (fresh biopsies), $20\mu\text{m}$ (pathological tissues), or $40\mu\text{m}$ (postmortem tissue for fiber-type-specific comparisons) thick sections were cut from the O.C.T.-embedded samples in a cryostat with -20°C chamber temperature and -16°C blade temperature. The sections were transferred and mounted on glass slides using the CryoJane Tape Transfer system and were either processed immediately or stored at -80°C in a tightly closed container until later use.

4.3 | Gel electrophoresis and Western blot

Thirty mg of freshly collected vastus lateralis muscle was homogenized in 0.6 mL lysis buffer (20 mM HEPES, 150 mM NaCl, 5 mM EDTA, 25 mM KF, 1 mM Na_3VO_4 , 20% (v/v) glycerol, 0.5% Triton X-100 and protease inhibitor (11836153001, Roche)) in a bead homogenizer. Samples were then rotated for 45 min at 4°C . Protein concentration was determined with Bradford assay, then two samples (lanes 1 and 2) were diluted to $20\text{ ng}/\mu\text{L}$, and two (lane 3 and 4) were processed without further dilution. The lysates were mixed with mercaptoethanol-containing $6\times$ Laemmli buffer (J61337.AC, Thermo Fisher Scientific) and boiled at 96°C for 6 min. $30\mu\text{L}$ of the samples were separated in 4%–20% Tris-glycine gels (4568094, Bio-Rad), next to Precision Plus Protein Dual Color Standards (1610374, Bio-Rad).

The separated proteins were blotted on nitrocellulose membranes. Blots were blocked in 3% BSA (bovine serum albumin)-0.1% Tween-PBS (phosphate-buffered saline) solution overnight and then were incubated with anti-SERCA1 (mouse monoclonal IgG1, VE121G9 clone, MA3-912, Thermo Fisher Scientific, $1\mu\text{g}/\text{mL}$) or anti-SERCA2 (rabbit monoclonal IgG, EPR9392 clone, ab150435, Abcam, $0.1\mu\text{g}/\text{mL}$) primary antibodies diluted in 0.3% BSA-0.1% Tween-PBS for 1 h. The membranes were washed in 0.1% Tween-PBS (3×10 minutes), then horseradish peroxidase (HRP)-conjugated anti-mouse and anti-rabbit antibodies (715-035-150, 715-035-152, Jackson ImmunoResearch), diluted in 0.3% BSA-0.1% Tween-PBS, were used to detect primary antibodies bound to the membrane. Excess of secondary antibodies was rinsed away with 0.1% Tween-PBS (3×10 min), then the target proteins were indirectly visualized with ECL substrate kits (1705060, Bio-Rad; 34095, Thermo Fisher

Scientific), and the chemiluminescent signal was captured with a GelDoc system (Bio-Rad). The images were exported in tiff format, and the brightness and contrast were adjusted in the Affinity Designer software.

4.4 | Immunohistochemistry

The slides were quickly warmed up to room temperature and then fixated in 4% formaldehyde-PBS for 20 min, followed by washing steps in PBS (3×5 min). $250\mu\text{L}$ blocking and permeabilization solution (BPS; 0.1% Triton X-100 and 4% normal goat or donkey serum in PBS), containing different combinations of primary antibodies anti-SERCA1 (mouse monoclonal IgG1, VE121G9 clone, MA3-912, Thermo Fisher Scientific, $2\mu\text{g}/\text{mL}$); anti-SERCA1 (rabbit polyclonal IgG, PA5-78835, Thermo Fisher Scientific, $2.5\mu\text{g}/\text{mL}$); anti-SERCA2 (rabbit monoclonal IgG, EPR9392 clone, ab150435, Abcam, $2\mu\text{g}/\text{mL}$); anti-MyHC1 (mouse monoclonal IgG2b, BA-D5 clone, DSHB, $1.25\mu\text{g}/\text{mL}$); anti-MyHC2A-2X (mouse monoclonal IgG1, SC-71 clone, DSHB, $2.5\mu\text{g}/\text{mL}$); anti-lamin A/C (mouse monoclonal IgG2b, 636 clone, sc-7292, Santa Cruz Biotechnology, $1\mu\text{g}/\text{mL}$); anti-lamin A/C (goat polyclonal IgG, N-18, sc-6215, $1\mu\text{g}/\text{mL}$); anti-PAX7 (mouse monoclonal IgG1, DSHB, $2.5\mu\text{g}/\text{mL}$); anti-CD45 (mouse monoclonal IgG1, MEM-28 clone, ab8216, $2\mu\text{g}/\text{mL}$) and anti-laminin (rabbit polyclonal, L9393, $1\mu\text{g}/\text{mL}$) was applied on each section, and the slides were then incubated in a humidified chamber at room temperature overnight. The following day, the sections were washed in PBS at room temperature (3×5 min), then $250\mu\text{L}$ PBS with different combinations of fluorescently labeled goat (A21121, A21127, A21242, A21245 or A31556, Thermo Fisher Scientific, $4\mu\text{g}/\text{mL}$) and donkey (711-166-152, 711-546-152, 715-166-150 or 715-546-151, Jackson ImmunoResearch, $1.5\mu\text{g}/\text{mL}$) secondary antibodies, Alexa Fluor 488- or 647-conjugated wheat germ agglutinin (WGA) (W11261 or W32466, Thermo Fisher Scientific, $5\mu\text{g}/\text{mL}$) and rhodamine-conjugated Ulex Europaeus Agglutinin I (UEA I) (RL-1062, Vector Laboratories, $10\mu\text{g}/\text{mL}$) was applied on the slides. The sections were incubated in a dark humidified chamber for 1 h at room temperature, with subsequent washing steps in PBS (3 times 5 min). The slides were submersed in PBS containing $0.2\mu\text{g}/\text{mL}$ DAPI (4,6-diamidino-2-phenylindole, Thermo Fisher Scientific) for 5 min between the second and third washing steps. Finally, glass coverslips were mounted on the sections using ProLong Gold Antifade Reagent (P10144, Thermo Fisher Scientific) and sealed with transparent nail polish after solidification. The stained slides were then stored at 4°C in dark.

4.5 | Confocal and epifluorescence microscopy and image processing

Areas of interest of transversally cut muscle regions were selected based on the perceived roundness of myofibers, minimal shift in the fiber border signal between different imaging planes, and a SERCA-labeling pattern consistent with perpendicular fiber orientation. Representative images of the stained skeletal muscle sections were captured by a Carl Zeiss LSM 700 laser scanning microscope with a Zen 2012 Black Edition software, using a Carl Zeiss Plan-Apochromat 20 \times /0.8, 40 \times /1.3 Oil DIC (UV)VIS-IR and 63 \times /1.4 Oil DIC objectives, with a 1024 \times 1024 pixel resolution and 4.1 μ m, 1.9 μ m and 1.1 μ m optical thickness, respectively. For the manual and automated image analysis, 3 \times 3 tile scans were captured with 20 \times magnification (0.156 μ m/pixel), 5 μ m optical thickness, and 2048 \times 2048 pixel resolution, and stitched with 10% overlap. For the determination of parameters including nuclear objects, the stitched scans were split into 9 image frames and processed sequentially, due to memory-related technical constraints. For scan-based analysis, the resolution of the tile scans was instead decreased to a quarter of the original (0.624 μ m/pixel) using bicubic interpolation, which saved processing time but had a negligible effect on the accuracy of purely myofiber-related parameters. For the comparison of imaging setups, an epifluorescence microscope (Axio Imager Z2 and Hamamatsu digital camera C11440, 20 \times objective) was used to generate 1900 \times 1900 pixel resolution image frames. Generated images were processed likewise.

Linear adjustments to the brightness and contrast of representative images were performed in Zen 2012 Black Edition and Affinity Designer. For images submitted to manual and automated analysis, care was taken not to oversaturate channels with information-bearing intensity values, as those were used to determine fiber- or myonucleus type. In the WGA or laminin channels, signal continuity and thus improved fiber object recognition was instead prioritized, and thus overexposure was allowed. All images were exported as both separate and merged channels in 8-bit png file format and submitted to manual or automated image analysis.

4.6 | Image analysis and data generation

The FiNuTyper workflow combines two open-source software with an in-house-developed Cellprofiler⁴⁹ pipeline. Firstly, nuclear object recognition from the DAPI signal was performed using the image style transfer-based neural network NucleAIzer,³⁰ on image frames where average nuclear diameter was set to 30 pixels (0.156 μ m/pixel).

Then, fiber objects were identified from the myofiber border marker WGA or laminin signal by Cellpose,²⁹ on both image frames and stitched scans, with an object diameter of 300 pixels (0.156 μ m/pixel, frame-based analysis) or 75 pixels (0.624 μ m/pixel, scan-based analysis), with a cytoplasm model and the model's predefined thresholds. The generated nucleus- and fiber object-masked images, along with a merged and separate channel images for SERCA1, SERCA2, WGA, and DAPI, were used as input in the Cellprofiler⁴⁹ pipeline for the frame-based analysis. No nuclear identification was performed as part of the scan-based analysis and thus no nucleus object-masked image was used in it. All parameters involving myonuclear values (type 1 myonuclear ratio, myonuclei per fiber, central myonuclei per fiber, myonuclear domain) were calculated from the high-resolution images with 0.156 μ m/pixel scaling, while purely fiber-related parameters (type 1 fiber ratio, cross-sectional area, grouped fiber ratio) were generated from the whole scans with decreased resolution with 0.624 μ m/pixel scaling, allowing for the analysis of a higher number of fibers in the same area of interest.

For fiber and myonucleus type determination, the intensities of the SERCA1 and SERCA2 signals were measured within the fiber and nucleus objects and quantified as average pixel intensity values (mean fiber or nucleus intensity). Fibers located on or close to the image borders were not identified by the pipeline, and fiber objects without measurable SERCA1 or SERCA2 signal were categorized as artifacts and excluded from subsequent analysis. After observing numerous (mainly type 2) fibers of uncommon shapes in our sections, we opted to completely exclude a roundness filter, commonly used in other automated pipelines, to avoid introducing type-specific technical bias in our data collection. The SERCA1 and SERCA2 intensity levels, used for fiber- and nucleotype gating, were calibrated for every experimental setting, using the histogram and density plot features of Cellprofiler Analyst.⁵⁰ For myonucleus type analysis, adjacency (adjacent object pixels or overlap) to a fiber object of the similar type was also considered. Based on the more distinct profile of SERCA2-positive fibers and myonuclei, fiber and nuclear objects co-expressing SERCA1 and SERCA2 were annotated as type 1.

Data used for subsequent analysis were extracted from the raw data file generated by the Cellprofiler⁴⁹ pipeline and compiled per individual or per-image scan (technical replicates). Individual numbers assigned to myofiber objects in the output dataset allowed for their unequivocal identification in the original images, making post hoc manual correction possible. Primary-derived values (number of fibers and myonuclei, fiber size, number of central myonuclei and number of grouped fibers) were compiled and averaged in a type-specific manner and were used to

calculate secondary derived values (type 1 fiber ratio, type 1 myonucleus ratio, myonucleus per fiber, myonuclear domain, grouped fiber ratio and grouped fiber size compared to average fiber size). These values were then used to characterize distinct fiber populations of the study subjects.

In the five additional, annotated pipelines, the following minor modifications were made: fiber-type annotation was performed exclusively based on the presence or absence of SERCA2 signal and the SERCA1 channel was replaced by UEA I (capillary identification), CD45 (leucocyte identification) or PAX7 (satellite cell identification). For capillary identification, nuclear objects were not considered, but UEA I-positive objects were annotated as capillaries using NucleAIzer (average object diameter set to 30 pixels). For leucocyte and satellite cell annotation, an overlap between DAPI and CD45 or Pax7 signals were considered. For a classical fiber-typing pipeline, the SERCA1 channel was exchanged to MyHC2A-2X and the SERCA2 to MyHC1 and the WGA to laminin. Finally, for the quantification of hybrid fibers and myonuclei, a parallel gating strategy for SERCA1 and SERCA2 and identification of double-positive objects was implemented.

The in-house-developed Cellprofiler module of the FiNuTyper pipeline is provided in File S1 (scan-based analysis) and File S2 (frame-based analysis), while technical notes and detailed instructions on how to run FiNuTyper is presented in File S3 (Files S1, S2 and S3 are provided as Mendeley data DOI: [10.17632/dfw8r794ph.3](https://doi.org/10.17632/dfw8r794ph.3)). A flowchart overview of the experimental protocol is visualized in Figure S5.

4.7 | Validation of MyHC and SERCA isoform co-expression

Overlap between the different MyHC and SERCA isoforms was evaluated in three male subjects of 25, 45, and 73 years of age, in immunostainings combining MyHC1-, MyHC2A-2X-, and SERCA1- or SERCA2-specific antibodies with fluorescently conjugated WGA. Three, approx. $0.9\text{ mm} \times 0.9\text{ mm}^2$ image scans (3×3 image frames with 10% overlap) were captured from each individual and were submitted to automated image analysis. Per scan, 213.78 ± 25.47 fibers for SERCA1 and 234.78 ± 20.41 fibers for SERCA2 validation were identified (mean \pm SD). Mean fiber intensities were measured in all three relevant channels. After manual exclusion of incorrectly outlined fiber objects, mean fiber intensity in the SERCA channel, measured in individual fiber objects, was plotted against the mean fiber intensity in the corresponding MyHC channel (SERCA1–MyHC2A-2X; SERCA2–MyHC1). Quadrant gates were defined by the lowermost intensity values in the clearly double-positive population, outlining

true-positive (TP; SERCA⁺–MyHC⁺), true-negative (TN; SERCA[–]–MyHC[–]), false-positive (SERCA⁺–MyHC[–]) and false-negative (SERCA[–]–MyHC⁺) fiber populations in each analyzed image scan. Sensitivity (TP/(TP + FN)), specificity (TN/(TN + FP)), positive predictive value (TP/(TP + FP)), and negative predictive value (TN/(TN + FN)) were calculated for each scan and then used to generate mean values for each subject separately. Final accuracy values were calculated as an average for the three subjects, displayed as mean \pm SD.

4.8 | Validation of fiber and myonucleus identification and CSA measurements

Fiber and myonucleus identification in postmortem psoas major and pectoralis major sections was evaluated by 2 independent operators, blind to the generated count, age, and sex of the subjects, in a 1/3 overlapping fashion ($n=57$ randomly selected, approx. $0.3 \times 0.3\text{ mm}^2$ image frames from ten subjects containing 880 fibers and 1179 myonuclei in total). Operator 1 validated 25 such frames, operator 2 validated 23 such frames, and 9 such frames were validated by both operators, the results of which were averaged for subsequent evaluation. Similar analysis of frozen sections of bioptic vastus lateralis muscle biopsies ($n=9$ randomly selected approx. $0.3 \times 0.3\text{ mm}^2$ image frames from three subjects containing 102 fibers and 304 myonuclei in total) was performed by a single operator. Validation of cross-sectional area measurements was performed separately in type 1 and type 2 fibers by a single, similarly blinded operator, both in postmortem ($n=35$ randomly selected, approx. $0.3 \times 0.3\text{ mm}^2$ image frames from 10 subjects containing 554 fibers in total) and bioptic samples ($n=9$ randomly selected, approx. $0.3 \times 0.3\text{ mm}^2$ image frames from three subjects containing 102 fibers in total), where mean CSA per-image frame values were calculated and displayed. The level of agreement between the manual and automated analyses was determined by calculating intraclass correlation coefficient (ICC) with 95% CI, and Bland–Altman analysis. Automated cross-sectional area measurement was also validated against manual quantification on the individual fiber level in a single image scan (9 stitched image frames, approx. $0.9 \times 0.9\text{ mm}^2$, $n=243$ fibers identified automatically; $n=254$ fibers evaluated manually).

4.9 | Statistics and data presentation

Intraclass correlation coefficient (ICC) analysis (two-way random effects, absolute agreement, single measures) was performed in IBM SPSS statistics 27 to assess comparability

between FiNuTyper-based and manual evaluation. Bland–Altman analysis for the validation dataset, paired data and group comparisons and visualization were performed in GraphPad Prism 9.3.1. Normal distribution of grouped datasets was analyzed by Shapiro–Wilk and Kolmogorov–Smirnov tests. Differences between groups were analyzed either with one-way ANOVA and Tukey's or Dunnett's post hoc test, or in case of two groups, paired *t* tests, Wilcoxon matched-pairs signed rank test, or Mann–Whitney *U* test, depending on analyzing paired or unpaired data points and the result of the previous normality test. Statistical significance was set to $p < 0.05$ and marked with asterisk (* $p < 0.05$; † $p \leq 0.01$; ‡ $p \leq 0.001$). For the validation analysis, per-image values were calculated and compared in all assessed parameters. For the analysis of the healthy subject cohort, all generated values were pooled on a per-subject basis. Central myonuclei per fiber values were calculated on a per-scan basis and compared between each pathological muscle sample and 3 healthy controls. Z-score was calculated from the $Z = (x - \mu) / \sigma$ formula. All data are presented as mean \pm SD.

ACKNOWLEDGMENTS

O.B. was supported by the Center for Regenerative Therapies Dresden, the Karolinska Institutet, the Swedish Research Council, the Ragnar Söderberg, the Åke Wiberg Foundation, and the LeDucq Foundation. S.M.R. was supported by a doctoral grant from Karolinska Institutet. C.J.S., E.B.E. and M.A.C. were supported by grants from the Swedish Research Council and the Swedish Research Council for Sport Science. We would like to thank Marion Baniol for her help with handling the postmortem muscle samples and discussions about the project, and Paula Heinke and Wouter Derks for their insightful comments on the manuscript.

CONFLICT OF INTEREST STATEMENT

The authors declare no competing interests.

DATA AVAILABILITY STATEMENT

Data and code used in this study are available on Mendeley data (DOI: [10.17632/dfw8r794ph.3](https://doi.org/10.17632/dfw8r794ph.3)) and will be made public upon publication.

ORCID

August Lundquist  <https://orcid.org/0000-0001-6524-9657>

Enikő Lázár  <https://orcid.org/0000-0001-8664-7531>

Eric B. Emanuelsson  <https://orcid.org/0000-0002-2746-8581>

Stefan M. Reitzner  <https://orcid.org/0000-0003-0151-2780>

Kanar Alkass  <https://orcid.org/0000-0002-9154-5393>

Henrik Druid  <https://orcid.org/0000-0002-9198-023X>

Susanne Petri  <https://orcid.org/0000-0002-9783-8584>

Carl J. Sundberg  <https://orcid.org/0000-0002-7000-466X>

Olaf Bergmann  <https://orcid.org/0000-0003-1065-4107>

REFERENCES

1. D'Antona G. The effect of ageing and immobilization on structure and function of human skeletal muscle fibres. *J Physiol.* 2003;552(2):499–511.
2. Lexell J, Taylor CC, Sjöström M. What is the cause of the ageing atrophy? *J Neurol Sci.* 1988;84(2–3):275–294.
3. Gundersen K, Bruusgaard JC, Egner IM, Eftestøl E, Bengtson M. Muscle memory: virtues of your youth? *J Physiol.* 2018;596(18):4289–4290. doi:10.1113/JP276354
4. Bruusgaard JC, Johansen IB, Egner IM, Rana ZA, Gundersen K. Myonuclei acquired by overload exercise precede hypertrophy and are not lost on detraining. *Proceedings of the National Academy of Sciences of the United States of America.* 2010;107(34):15111–15116. doi:10.1073/pnas.0913935107
5. Snijders T, Aussieker T, Holwerda A, Parise G, Loon LJC, Verdijk LB. The concept of skeletal muscle memory: evidence from animal and human studies. *Acta Physiologica.* 2020;229(3):e13465. doi:10.1111/apha.13465
6. Nilwik R, Snijders T, Leenders M, et al. The decline in skeletal muscle mass with aging is mainly attributed to a reduction in type II muscle fiber size. *Exp Gerontol.* 2013;48(5):492–498. doi:10.1016/j.exger.2013.02.012
7. Damas F, Libardi CA, Ugrinowitsch C, et al. Early- and later-phases satellite cell responses and myonuclear content with resistance training in young men. *PLoS One.* 2018;13(1):e0191039. doi:10.1371/journal.pone.0191039
8. Allen DL, Yasui W, Tanaka T, et al. Myonuclear number and myosin heavy chain expression in rat soleus single muscle fibers after spaceflight. *J Appl Physiol.* 1996;81(1):145–151. doi:10.1152/jappl.1996.81.1.145
9. Lavin KM, Sealon SC, McDonald M-LN, et al. Skeletal muscle transcriptional networks linked to type I myofiber grouping in Parkinson's disease. *J Appl Physiol.* 2020;128(2):229–240.
10. Fischer LR, Culver DG, Tennant P, et al. Amyotrophic lateral sclerosis is a distal axonopathy: evidence in mice and man. *Exp Neurol.* 2004;185(2):232–240.
11. Mayeuf-Louchart A, Hardy D, Thorel Q, et al. MuscleJ: a high-content analysis method to study skeletal muscle with a new Fiji tool. *Skelet Muscle.* 2018;8(1):25. doi:10.1186/s13395-018-0171-0
12. Al-Shammari AA, Kissane RWP, Holbek S, et al. Integrated method for quantitative morphometry and oxygen transport modeling in striated muscle. *J Appl Physiol.* 2019;126(3):544–557. doi:10.1152/japplphysiol.00170.2018
13. Babcock LW, Hanna AD, Agha NH, Hamilton SL. MyoSight—semi-automated image analysis of skeletal muscle cross sections. *Skelet Muscle.* 2020;10(1):33. doi:10.1186/s13395-020-00250-5
14. Waisman A, Norris AM, Elías Costa M, Kopinke D. Automatic and unbiased segmentation and quantification of myofibers in skeletal muscle. *Sci Rep.* 2021;11(1):11793. doi:10.1038/s41598-021-91191-6
15. Desgeorges T, Liot S, Lyon S, et al. Open-CSAM, a new tool for semi-automated analysis of myofiber cross-sectional area in regenerating adult skeletal muscle. *Skelet Muscle.* 2019;9(1):2. doi:10.1186/s13395-018-0186-6

16. Sanz G, Martínez-Aranda LM, Tesch PA, Fernandez-Gonzalo R, Lundberg TR. Muscle2View, a CellProfiler pipeline for detection of the capillary-to-muscle fiber interface and high-content quantification of fiber type-specific histology. *J Appl Physiol*. 2019;127(6):1698-1709. doi:10.1152/jappphysiol.00257.2019
17. Smith LR, Barton ER. SMASH – semi-automatic muscle analysis using segmentation of histology: a MATLAB application. *Skelet Muscle*. 2014;4(1):21. doi:10.1186/2044-5040-4-21
18. Kastenschmidt JM, Ellefsen KL, Mannaa AH, et al. QuantiMus: a machine learning-based approach for high precision analysis of skeletal muscle morphology. *Front Physiol*. 2019;10:1416. doi:10.3389/fphys.2019.01416
19. Encarnacion-Rivera L, Foltz S, Hartzell HC, Choo H. Myosoft: an automated muscle histology analysis tool using machine learning algorithm utilizing FIJI/ImageJ software. *PLoS One*. 2020;15(3):e0229041. doi:10.1371/journal.pone.0229041
20. Wen Y, Murach KA, Vechetti IJ, et al. MyoVision: software for automated high-content analysis of skeletal muscle immunohistochemistry. *J Appl Physiol*. 2018;124(1):40-51. doi:10.1152/jappphysiol.00762.2017
21. Stevens CR, Berenson J, Sledziona M, Moore TP, Dong L, Cheetham J. Approach for semi-automated measurement of fiber diameter in murine and canine skeletal muscle. *PLoS One*. 2020;15(12):e0243163. doi:10.1371/journal.pone.0243163
22. Viggars MR, Wen Y, Peterson CA, Jarvis JC. Automated cross-sectional analysis of trained, severely atrophied, and recovering rat skeletal muscles using MyoVision 2.0. *J Appl Physiol*. 2022;132(3):593-610.
23. Kim Y-J, Brox T, Feiden W, Weickert J. Fully automated segmentation and morphometrical analysis of muscle fiber images. *Cytometry A*. 2007;71A(1):8-15.
24. Klemencic A, Kovacic S, Pernus F. Automated segmentation of muscle fiber images using active contour models. *Cytometry*. 1998;32(4):317-326.
25. Winje IM, Bengtson M, Eftestøl E, Juvkam I, Bruusgaard JC, Gundersen K. Specific labelling of myonuclei by an antibody against pericentriolar material 1 on skeletal muscle tissue sections. *Acta Physiol*. 2018;223(4):e13034.
26. Murach KA, Englund DA, Dupont-Versteegden EE, McCarthy JJ, Peterson CA. Myonuclear domain flexibility challenges rigid assumptions on satellite cell contribution to skeletal muscle fiber hypertrophy. *Front Physiol*. 2018;9:635. doi:10.3389/fphys.2018.00635
27. Herman-Montemayor JR, Hikida RS, Staron RS. Early-phase satellite cell and myonuclear domain adaptations to slow-speed vs. traditional resistance training programs. *J Strength Cond Res*. 2015;29(11):3105-3114. doi:10.1519/JSC.0000000000000925
28. Xu H, Van Remmen H. The SarcoEndoplasmic reticulum calcium ATPase (SERCA) pump: a potential target for intervention in aging and skeletal muscle pathologies. *Skelet Muscle*. 2021;11(1):25.
29. Stringer C, Wang T, Michaelos M, Pachitariu M. Cellpose: a generalist algorithm for cellular segmentation. *Nat Methods*. 2021;18(1):100-106.
30. Hollandi R, Szkalitsy A, Toth T, et al. nucleAIzer: a parameter-free deep learning framework for nucleus segmentation using image style transfer. *Cell Syst*. 2020;10(5):453-458.e6. doi:10.1016/j.cels.2020.04.003
31. Koo TK, Li MY. A guideline of selecting and reporting intraclass correlation coefficients for reliability research. *J Chiropr Med*. 2016;15(2):155-163.
32. Mosole S, Carraro U, Kern H, Loeffler S, Zampieri S. Use it or lose it: tonic activity of slow motoneurons promotes their survival and preferentially increases slow fiber-type groupings in muscles of old lifelong recreational sportsmen. *Eur J Transl Myol*. 2016;26(4):5972.
33. Kelly NA, Hammond KG, Stec MJ, et al. Quantification and characterization of grouped type I myofibers in human aging. *Muscle Nerve*. 2018;57(1):E52-E59. doi:10.1002/mus.25711
34. Conceição MS, Vechin FC, Lixandrão M, et al. Muscle fiber hypertrophy and myonuclei addition: a systematic review and meta-analysis. *Med Sci Sports Exerc*. 2018;50(7):1385-1393.
35. Snijders T, Holwerda AM, van Loon LJC, Verdijk LB. Myonuclear content and domain size in small versus large muscle fibres in response to 12 weeks of resistance exercise training in older adults. *Acta Physiol (Oxf)*. 2021;231(4):e13599.
36. Gouzi F, Maury J, Molinari N, et al. Reference values for vastus lateralis fiber type proportion and fiber size. *J Appl Physiol*. 2014;116(2):228.
37. Jensen L, Jørgensen LH, Bech RD, Frandsen U, Schröder HD. Skeletal muscle remodelling as a function of disease progression in amyotrophic lateral sclerosis. *Biomed Res Int*. 2016;2016:5930621.
38. Arnardottir S. Sporadic inclusion body myositis: morphology, regeneration, and cytoskeletal structure of muscle fibres. *J Neurol Neurosurg Psychiatry*. 2004;75(6):917-920.
39. Verma A, Bradley WG, Soule NW, et al. Quantitative morphometric study of muscle in inclusion body myositis. *J Neurol Sci*. 1992;112(1-2):192-198.
40. Ørtenblad N, Nielsen J, Boushel R, Söderlund K, Saltin B, Holmberg H-C. The muscle fiber profiles, mitochondrial content, and enzyme activities of the exceptionally well-trained arm and leg muscles of elite cross-country skiers. *Front Physiol*. 2018;9:1031. doi:10.3389/fphys.2018.01031
41. Pereyra AS, Lin C-T, Sanchez DM, et al. Skeletal muscle undergoes fiber type metabolic switch without myosin heavy chain switch in response to defective fatty acid oxidation. *Mol Metab*. 2022;59:101456.
42. Talmadge RJ, Castro MJ, Apple DF, Dudley GA. Phenotypic adaptations in human muscle fibers 6 and 24 wk after spinal cord injury. *J Appl Physiol*. 2002;92(1):147-154.
43. Morissette MP, Susser SE, Stammers AN, et al. Differential regulation of the fiber type-specific gene expression of the sarcoplasmic reticulum calcium-ATPase isoforms induced by exercise training. *J Appl Physiol*. 2014;117(5):544-555.
44. Ranganathan P, Pramesh C, Aggarwal R. Common pitfalls in statistical analysis: measures of agreement. *Perspect Clin Res*. 2017;8(4):187-191.
45. Krivickas LS, Yang J-I, Kim S-K, Frontera WR. Skeletal muscle fiber function and rate of disease progression in amyotrophic lateral sclerosis. *Muscle Nerve*. 2002;26(5):636-643.
46. Hegedus J, Putman CT, Gordon T. Time course of preferential motor unit loss in the SOD1G93A mouse model of amyotrophic lateral sclerosis. *Neurobiol Dis*. 2007;28(2):154-164.
47. Hegedus J, Putman CT, Tyreman N, Gordon T. Preferential motor unit loss in the SOD1G93A transgenic mouse model of amyotrophic lateral sclerosis. *J Physiol*. 2008;586(14):3337-3351.

48. Achari AN, Anderson MS. Myopathic changes in amyotrophic lateral sclerosis. Pathologic analysis of muscle biopsy changes in 111 cases. *Neurology*. 1974;24(5):477-481.
49. McQuin C, Goodman A, Chernyshev V, et al. CellProfiler 3.0: next-generation image processing for biology. *PLoS Biol*. 2018;16(7):e2005970. doi:10.1371/journal.pbio.2005970
50. Dao D, Fraser AN, Hung J, Ljosa V, Singh S, Carpenter AE. CellProfiler analyst: interactive data exploration, analysis and classification of large biological image sets. *Bioinformatics*. 2016;32(20):3210-3212. doi:10.1093/bioinformatics/btw390

SUPPORTING INFORMATION

Additional supporting information can be found online in the Supporting Information section at the end of this article.

How to cite this article: Lundquist A, Lázár E, Han NS, et al. FiNuTyper: Design and validation of an automated deep learning-based platform for simultaneous fiber and nucleus type analysis in human skeletal muscle. *Acta Physiol*. 2023;239:e13982. doi:10.1111/apha.13982